Available online at www.sciencedirect.com
ScienceDirect
Journal of Computational Physics 220 (2006) 19–40
JOURNAL OF COMPUTATIONAL PHYSICS
www.elsevier.com/locate/jcp

A grid and flow adaptive wall-function method for RANS turbulence modelling

Tobias Knopp *, Thomas Alrutz, Dieter Schwamborn

DLR (German Aerospace Center), Institute of Aerodynamics and Flow Technology, Bunsenstr. 10, 37073 Göttingen, Germany

Received 30 September 2005; received in revised form 1 May 2006; accepted 2 May 2006
Available online 22 June 2006

Abstract

This paper presents a grid and flow adaptive wall-function method for RANS turbulence modelling with emphasis on aerodynamic flows. A near-wall grid adaptation technique ensures a locally appropriate resolution depending on both the near-wall flow physics to be captured and the range of validity of the wall-function model. The near-wall RANS solutions of the Spalart–Allmaras and SST k–ω turbulence model are investigated near stagnation points and subsequent not yet fully developed turbulent flow, and in regions of adverse pressure gradient before separation. These are compared with the corresponding turbulence model specific universal wall-functions and suggestions for the design of wall-function methods for non-equilibrium flows are given. Regions of non-equilibrium flow are detected by a flow based sensor and near-wall grid adaptation is then made possible due to the hybrid character of the wall-functions.

PACS: 47.27.Eq; 47.27.Jv; 47.27.Nz; 47.85.Gj

MSC: 65B99; 65N55; 76F40; 76F55; 76M12

Keywords: Wall function; RANS turbulence modelling; Domain decomposition; Grid adaptation

1. Introduction

In order to ensure both accuracy and efficiency of a simulation of complex flows, a computational method has to choose (i) an appropriate the level of complexity for physical/mathematical description and (ii) a numerical resolution adapted to the flow structures to be resolved and to the flow physics to be modelled. In the present paper, the two levels of flow description are hybrid universal wall functions and the full RANS and turbulence model equations. The numerical near-wall resolution depends on the near-wall flow structures to be resolved, on the range of validity of the wall-function model applied, and on the convergence acceleration for the numerical method aspired. Near-wall grid adaptation is made possible due to the hybrid character of the wall-function method.

* Corresponding author. Tel.: +49 551 7092451; fax: +49 551 7092416.
E-mail address: Tobias.Knopp@dlr.de (T. Knopp).

0021-9991/$ - see front matter
doi:10.1016/j.jcp.2006.05.003

The aim of *hybrid* (or *adaptive*) *wall-functions* is to provide a boundary condition at solid walls that enables flow solutions independent of the location of the first grid node above the wall, in particular concerning surface coefficients like pressure, skin friction and heat transfer. Denote $y^+(1)$ the distance of the first off-wall node in viscous length-scales. *Low-Re boundary conditions* impose no-slip at the wall and the RANS equations are integrated down to the wall, e.g., for the k–ω, Spalart–Allmaras and v^2–f model, which requires a so-called *low-Reynolds grid* with $y^+(1) \approx 1$. *High-Re boundary conditions* are used in standard wall-function formulations and prescribe the wall-shear stress and no-penetration at the wall. The RANS equations are solved only down to the inner part of the logarithmic layer and matched with the logarithmic law of the wall at the first grid node above the wall. High-Re boundary conditions require a so-called *high-Reynolds grid* with $y^+(1)$ being located in the log-layer. Moreover, we introduce the term *intermediate-Re* grid to refer to the region between viscous sublayer and log-layer, i.e., the buffer layer.

Wall functions are based on the fact that for incompressible flows the solution between the wall and the outer edge of the logarithmic layer is *universal* at least in quasi-equilibrium boundary layers. As the term "law of the wall" was originally used for the universal log-layer solution, the terms "hybrid law of the wall" or "adaptive law of the wall" have been proposed to stress validity in the entire near-wall region. The debate on whether the (hybrid) law of the wall does not vary in pressure gradients is still open (see [1,2] and references therein). Regarding the goal of grid-independent wall-functions, however, it is the *behaviour* of RANS turbulence models in flows with pressure gradients which is of major importance. In this paper very satisfying results are obtained without explicitly taking into account the pressure gradient.

Computational fluid dynamics (CFD) has been reaching more and more maturity as a general predictive tool in industry with "sensible" reliability. Despite the fast increase in available computing resources during the last decades, the huge computing costs are still a major limiting factor in the "appropriate" usage (in terms of the numerical discretization error) of CFD tools in industry, in particular for unsteady calculations. An additional need for improving performance arises as CFD-solvers are more and more used as part of optimization processes. This requires fast CFD-solutions for a large number of geometrical configurations without loss in accuracy.

Low-Re grids require a large number of grid points in the near-wall region. E.g., for an airfoil flow at Reynolds number 6×10^6, a low-Re grid requires around 35 nodes in wall normal direction to resolve the boundary layer whereas a high-Re grid with $y^+(1) \approx 70$ can do with 17. Moreover, numerical stiffness problems arise on low-Re grids due to the large velocity gradients at the wall in conjunction with the small cell height, which imply a very small pseudo time-step width and a large number of solver iterations. Moreover, the generation of intermediate- and high-Re grids is much simpler. As a final remark on the areas of relevance, wall-functions have been employed successfully as near-wall model for large-eddy simulation [3].

Albeit wall-functions are still strongly relevant in CFD and despite the more than 30 years enduring efforts in this topic, most of the current approaches e.g. [4–7] seem to be suboptimal in the sense that their wall-functions are not consistent with the turbulence model used for the global flow problem. This causes a strong dependence of the numerical results on the location of the first off-wall grid node which leads to poor results in flows with separation. To the author's best knowledge the first paper which addressed and solved this issue of consistency at least for flows close to equilibrium is the one by [8].

In the present paper the focus is on non-equilibrium flows with emphasis on aerodynamics with (i) stagnation points and laminar/not fully developed turbulent flow, (ii) regions of significant pressure gradient parameter due to a strong (adverse) pressure gradient at a typically moderate Reynolds number and (iii) regions of separation and reattachment. These flow situations are very important not only for flows around airfoils and rotor blades, but even more for complex aircraft configurations with flaps, engines, etc. For such flows, this paper proposes techniques for significant further improvement of the results in [9].

We restrict ourselves to flows in the subsonic and transonic regime. For high-speed flows at large Mach numbers with very large temperature differences near walls, the physics involved do not seem to be yet completely understood. Based on the pioneering work [10], compressible wall-functions have been proposed [11,12] but require further improvement.

The high-Re grid condition is violated in separated flows due to strong adverse pressure gradient when pressure increases smoothly, e.g. for the flow over an airfoil in highlift configuration, the flow over a wind turbine or in a diffusor. As the separation point is approached, $y^+(1)$ goes to zero as friction velocity is zero at the

separation point. Hence a grid which is of high-Re type far upstream of separation violates more and more the high-Re constraint as the separation point is approached. Then classical high-Re wall-functions inevitably fail. For hybrid but inconsistent wall-functions [4,6,7] the grid-dependence causes a modelling error which accumulates as the separation point is approached and results in poor predictions.

On high-Re grids, the results for turbulence model consistent wall-functions still deviate from the corresponding low-Re solution in the flow situations (i)–(iii) mentioned above. As in these situations the wall-functions are still very close to the low-Re solution for $y^+(1) \lessapprox 10$, we detect these regions using a flow-based sensor and use a $y^+(1)$-grid-adaptation method to ensure locally a low-Re or intermediate-Re grid, which is allowed by the hybrid nature of consistent wall-functions.

This paper is organized as follows. In Section 2 the governing equations for compressible fluid flow and RANS turbulence modelling are given. In Section 3 the wall-function method is formulated as a domain decomposition with full overlap in the near-wall region. Universal wall-functions are proposed in a new closed form and the underlying modelling assumptions are investigated, see Sections 4 and 5. The combination of wall-functions and wall-normal grid adaptation with a flow-based sensor is presented in Section 6. In Section 7 the numerical method is described. Numerical results are given in Sections 8 and 9.

2. The governing equations of compressible turbulent fluid flow

2.1. RANS equations for compressible flows

We consider the steady-state Favre-averaged compressible Navier–Stokes equations in a bounded Lipschitz domain $\Omega \subset \mathbb{R}^d$ $(d = 2, 3)$. We use the eddy-viscosity assumption for the Reynolds-stress tensor and the gradient-diffusion approximation for the turbulent heat-flux vector. The *low-Re formulation* reads as follows: We seek velocity $\vec{u} : \Omega \to \mathbb{R}^d$, density $\rho : \Omega \to \mathbb{R}$, pressure $p : \Omega \to \mathbb{R}$, and temperature $\theta : \Omega \to \mathbb{R}$ s.t.

$$\vec{\nabla} \cdot (\rho \vec{u}) = 0 \quad \text{in } \Omega, \tag{1}$$

$$\vec{\nabla} \cdot (\rho \vec{u} \otimes \vec{u}) - \vec{\nabla} \cdot [2\mu_e \mathbb{T}(\vec{u})] + \vec{\nabla} p = 0 \quad \text{in } \Omega, \tag{2}$$

$$\vec{\nabla} \cdot \left(\rho \vec{u} \left(h + \frac{1}{2} \vec{u} \cdot \vec{u} \right) \right) - \vec{\nabla} \cdot [\vec{u}(2\mu_e \mathbb{T}(\vec{u}))] - \vec{\nabla} \cdot (\kappa_e \vec{\nabla} \theta) = 0 \quad \text{in } \Omega \tag{3}$$

with the following boundary conditions on solid walls Γ_w

$$\vec{u} = \vec{0} \quad \text{on } \Gamma_w, \tag{4}$$

$$\text{(i) } \kappa_e \vec{\nabla} \theta \cdot \vec{n} = 0 \quad \text{on } \Gamma_w \text{ or (ii) } \theta = \theta_w \quad \text{on } \Gamma_w. \tag{5}$$

We use the Sutherland law for molecular viscosity μ and the equations of state $p = \rho R \theta$, $e = c_v \theta$ for specific internal energy, and $h = e + p/\rho = c_p \theta$ for specific enthalpy, with gas constant R, specific heat at constant volume c_v, specific heat at constant pressure c_p, strain rate tensor $\mathbb{T}(\vec{u})$

$$\mathbb{T}(\vec{u}) \equiv \mathbb{S}(\vec{u}) - \frac{1}{3} \vec{\nabla} \cdot \vec{u} \mathbb{I}, \quad \text{with } \mathbb{S}(\vec{u}) = \frac{1}{2} (\vec{\nabla} \vec{u} + (\vec{\nabla} \vec{u})^T),$$

effective viscosity $\mu_e = \mu + \mu_t$ and effective thermal conductivity $\kappa_e = \kappa + \kappa_t$ where $\kappa = c_p \mu / Pr$, $\kappa_t = c_p \mu_t / Pr_t$ with laminar and turbulent Prandtl numbers $Pr = 0.72$ and $Pr_t = 0.85$ resp.

2.2. Spalart–Allmaras turbulence model

The Spalart–Allmaras type one-equation turbulence models [13,14] compute the eddy viscosity μ_t from the relation $\mu_t = \rho \nu_t$ with $\nu_t = f_{v1} \max(\tilde{\nu}; 0)$ where $\tilde{\nu}$ is the solution of the transport equation

$$\vec{\nabla} \cdot (\rho \vec{u} \tilde{\nu}) - \vec{\nabla} \cdot \left(\frac{\mu + \rho \tilde{\nu}}{\sigma} \vec{\nabla} \tilde{\nu} \right) - \rho \frac{c_{b2}}{\sigma} (\vec{\nabla} \tilde{\nu}) \cdot (\vec{\nabla} \tilde{\nu}) = c_{b1} \rho \tilde{S} \tilde{\nu} - c_{w1} \rho f_w \left(\frac{\tilde{\nu}}{d} \right)^2$$

with d being the distance to the closest wall and near-wall damping function $f_{v1} = \chi^3 / (\chi^3 + c_{v1}^3)$ with $\chi = \tilde{\nu} / \nu$. On walls $\tilde{\nu} = 0$ is prescribed.

2.3. Wilcox k–ω turbulence model

Several k–ω model versions (e.g. [15–18]) have evolved from the original proposal [11] where $\mu_t = \rho k/\omega$ and k, ω are the solution of

$$\vec{\nabla}\cdot(\rho\vec{u}k) - \vec{\nabla}\cdot((\mu+\sigma_k\mu_t)\vec{\nabla}k) = 2\mu_t\mathbb{T}(\vec{u}) : \vec{\nabla}\vec{u} - \beta_k\rho k\omega,$$
$$\vec{\nabla}\cdot(\rho\vec{u}\omega) - \vec{\nabla}\cdot((\mu+\sigma_\omega\mu_t)\vec{\nabla}\omega) = 2\gamma\rho\mathbb{T}(\vec{u}) : \vec{\nabla}\vec{u} - \beta_\omega\rho\omega^2$$

with constants β_k, β_ω, γ, σ_k and σ_ω. We impose $k = 0$ on solid walls. The solution for ω from asymptotic theory (cf. [11]) is given by $\omega = 6\nu/(\beta_\omega y^2)$ and becomes singular at the wall. In industrial RANS solvers, the boundary condition equation (26) in [15] (abbreviated Menter b.c.) is very popular. Alternatively, Wilcox [11] suggests to prescribe ω at the first grid point above the wall Γ_δ at wall-distance y_δ located in the viscous sublayer (Wilcox b.c.):

$$\text{Menter b.c.} : \omega = C_w\omega_\delta \quad \text{on } \Gamma_w, \quad \text{with } \omega_\delta = \frac{6\nu}{\beta_\omega y_\delta^2}, \quad C_w = 10, \tag{6}$$

$$\text{Wilcox b.c.} : \omega = \omega_\delta \quad \text{on } \Gamma_\delta, \quad \text{with } \omega_\delta = \frac{6\nu}{\beta_\omega y_\delta^2}. \tag{7}$$

3. The wall-function concept

3.1. Domain decomposition method with full overlap in the near-wall region

To remedy the no-slip condition (4) instead of solving (1)–(5) in the computational domain Ω we consider a modified problem based on a domain-decomposition with full overlap [19]. Denote $\Omega_\delta \subset \Omega$ the near-wall region (Fig. 1 (left)) with artificial inner boundary Γ_δ located within or below the log-layer (Fig. 1 (right)). Then we divide (1)–(5) into two problems: a *global flow* problem to be solved in the whole domain Ω with modified wall boundary condition (the wall-shear stress is imposed instead of no-slip) and a *boundary-layer problem* to be solved in the near-wall region Ω_δ, see also [19,20]. Then the *wall-function or hybrid-Re formulation* reads as follows:

We seek a *global solution* $\rho : \Omega \to \mathbb{R}$, $\vec{u} : \Omega \to \mathbb{R}^d$, $p : \Omega \to \mathbb{R}$, $\theta : \Omega \to \mathbb{R}$ s.t.

$$\vec{\nabla}\cdot(\rho\vec{u}) = 0 \quad \text{in } \Omega, \tag{8}$$

$$\vec{\nabla}\cdot(\rho\vec{u}\otimes\vec{u}) - \vec{\nabla}\cdot(2\mu_e\mathbb{T}(\vec{u})) + \vec{\nabla}p = 0 \quad \text{in } \Omega, \tag{9}$$

$$\vec{\nabla}\cdot\left(\rho\vec{u}\left(h + \frac{1}{2}\vec{u}\cdot\vec{u}\right)\right) - \vec{\nabla}\cdot[\vec{u}(2\mu_e\mathbb{T}(\vec{u}))] - \vec{\nabla}\cdot(\kappa_e\vec{\nabla}\theta) = 0 \quad \text{in } \Omega \tag{10}$$

with the following modified boundary conditions on Γ_w

$$\vec{u}\cdot\vec{n} = 0, (\mathbb{I} - \vec{n}\otimes\vec{n})2\mu_e\mathbb{T}(\vec{u})\vec{n} = -\tau_w(\vec{u}^{bl}, \rho^{bl}, \theta^{bl})\vec{u}_t \quad \text{on } \Gamma_w \tag{11}$$

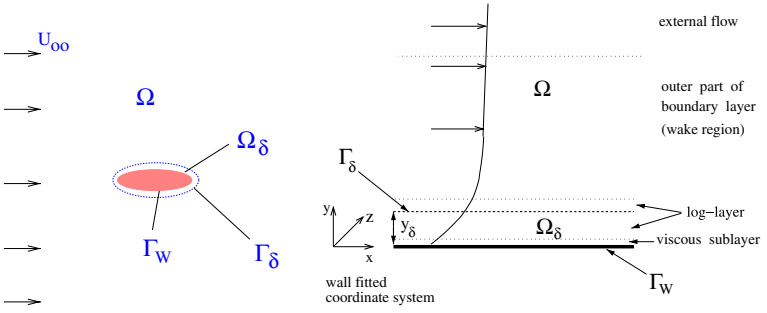

Fig. 1. Domain decomposition with full overlap in the near-wall region.

$$\text{(i) } \kappa_e \vec{\nabla}\theta \cdot \vec{n} = 0 \quad \text{on } \Gamma_w, \tag{12}$$

or

$$\text{(ii) } \kappa_e \vec{\nabla}\theta \cdot \vec{n} = -\dot{q}_w(\vec{u}^{bl}, \rho^{bl}, \theta^{bl}) \quad \text{on } \Gamma_w, \tag{13}$$

where $\mathbb{I} - \vec{n} \otimes \vec{n}$ is a projection operator onto the tangential space of Γ_w and

$$\vec{u}_t = \frac{\vec{v}_t}{|\vec{v}_t|}, \quad \vec{v}_t = (\mathbb{I} - \vec{n} \otimes \vec{n})\vec{u}|_{\Gamma_\delta} \quad \text{with } (\mathbb{I} - \vec{n} \otimes \vec{n})_{ij} = \delta_{ij} - n_i n_j \tag{14}$$

with $\delta_{ij} = 1$ if $i = j$ and zero otherwise ($1 \leqslant i,j \leqslant d$). The wall-shear stress τ_w and the turbulent heat flux $\dot{q}_w$ are calculated from

$$\tau_w(\vec{u}^{bl}, \rho^{bl}, \theta^{bl})\vec{u}_t = -(\mathbb{I} - \vec{n} \otimes \vec{n}) 2\mu_e^{bl} \mathbb{T}(\vec{u}^{bl})\vec{n} \quad \text{on } \Gamma_w, \tag{15}$$

$$\dot{q}_w(\vec{u}^{bl}, \rho^{bl}, \theta^{bl}) = -\kappa_e^{bl} \vec{\nabla}\theta^{bl} \cdot \vec{n} \quad \text{on } \Gamma_w, \tag{16}$$

where the *boundary layer solution* $\vec{u}^{bl} : \Omega_\delta \to \mathbb{R}^d$, $\rho^{bl} : \Omega_\delta \to \mathbb{R}$, $p^{bl} : \Omega_\delta \to \mathbb{R}$, and $\theta^{bl} : \Omega_\delta \to \mathbb{R}$ is determined by

$$\vec{\nabla} \cdot (\rho^{bl}\vec{u}^{bl}) = 0 \quad \text{in } \Omega_\delta, \tag{17}$$

$$\vec{\nabla} \cdot (\rho^{bl}\vec{u}^{bl} \otimes \vec{u}^{bl}) - \vec{\nabla} \cdot (2\mu_e^{bl}\mathbb{T}(\vec{u}^{bl})) + \vec{\nabla}p^{bl} = 0 \quad \text{in } \Omega_\delta, \tag{18}$$

$$\vec{\nabla} \cdot \left(\rho^{bl}\vec{u}^{bl}\left(h^{bl} + \frac{1}{2}\vec{u}^{bl} \cdot \vec{u}^{bl} \right) \right) - \vec{\nabla} \cdot \left[\vec{u}^{bl}\left(2\mu_e^{bl}\mathbb{T}(\vec{u}^{bl})\right) \right] - \vec{\nabla} \cdot \left(\kappa_e^{bl}\vec{\nabla}\theta^{bl} \right) = 0 \quad \text{in } \Omega_\delta \tag{19}$$

with the boundary conditions

$$\vec{u}^{bl} = \vec{0} \quad \text{on } \Gamma_w, \tag{20}$$

$$\text{(i) } \kappa_e^{bl}\vec{\nabla}\theta^{bl} \cdot \vec{n} = 0 \quad \text{on } \Gamma_w \quad \text{or (ii) } \theta^{bl} = \theta_w \quad \text{on } \Gamma_w, \tag{21}$$

$$\theta^{bl} = \theta, \quad \vec{u}^{bl} = \vec{u} \quad \text{on } \Gamma_\delta. \tag{22}$$

The boundary layer solution satisfies the original boundary conditions (4), (5) on Γ_w and is matched with the global solution on Γ_δ.

A wall-function method is called *grid independent* (or *hybrid* or *adaptive*) if (i) the method is well-defined for any location of Γ_δ and (ii) the solution of (8)–(22) is independent of the location of Γ_δ (provided Γ_δ resides in the log-layer or below). In particular, this definition implies grid-independence of surface quantities like pressure coefficient c_p and skin-friction coefficient c_f.

In practice, the aim is to avoid solving the full compressible RANS plus turbulence model equations (17)–(22) in the near-wall region and hence standard boundary layer approximations are used.

3.2. Boundary-layer approximation for universal wall functions

Numerical tests show that effects of compressibility in the near-wall region are negligible for Mach numbers smaller 1.4. Moreover, the near-wall attached flow is already surprisingly well described by the one-dimensional boundary layer equations, except very close to flow separation and reattachment, where a two-dimensional boundary layer model is superior.

Then, instead of (17)–(22) in Ω_δ, for each $\vec{x}_W \in \Gamma_W$ and given $u_\delta = \|\vec{v}_t\|$ from the global RANS solution by (14), seek the wall-parallel component of velocity $u^{bl}(y)$ such that

$$\frac{d}{dy}\left((\nu + \nu_t^{bl})\frac{du^{bl}}{dy} \right) = f \quad \text{in } \{\vec{x}_W - y\vec{n} | y \in (0, y_\delta)\}, \tag{23}$$

$$u^{bl}(0) = 0, \quad u^{bl}(y_\delta) = u_\delta \equiv \|\vec{v}_t\|, \tag{24}$$

where $f = 0$ or $f = 1/\rho\, dp/dx$ assumed to be independent of y and given from the global RANS solution at Γ_δ. Therein, denote $y_\delta = \text{dist}(\vec{x}_W, \Gamma_\delta)$. The variant $f = 0$ is called equilibrium stress balance model leading to universal near-wall solutions.

It is well known that for equilibrium boundary layers, e.g., the flow over a flat plate at zero pressure gradient, in the region between the wall and the outer edge of the logarithmic layer, the profiles for mean flow u and turbulence quantities k, ω, $\tilde{\nu}$ and hence ν_t are universal, i.e., they collapse when scaled with friction velocity u_τ and viscosity $\nu = \mu/\rho$

$$u^+ = \frac{u}{u_\tau}, \quad y^+ = \frac{y u_\tau}{\nu}, \quad \nu_t^+ = \frac{\nu_t}{\nu}, \quad p^+ = \frac{\nu}{\rho u_\tau^3}\frac{\mathrm{d}p}{\mathrm{d}x}, \quad k^+ = \frac{k}{u_\tau^2}, \quad \omega^+ = \frac{\omega \nu}{u_\tau^2}. \tag{25}$$

These universal near-wall profiles may be obtained by integration of (23) with $f = 0$ and the corresponding 1D boundary-layer equations for k and ω resp. $\tilde{\nu}$.

Eq. (23) in plus-units reveals that it is the pressure gradient parameter p^+ which controls the validity of the equilibrium stress balance assumption

$$\left(1 + \nu_t^+\right)\frac{\mathrm{d}u^+}{\mathrm{d}y^+} = 1 + p^+ y^+ \quad \text{in } (0, y_\delta^+). \tag{26}$$

4. Validation of the boundary layer approximation for aerodynamic flows

In this section, we investigate the near-wall behaviour of the SA-E and SST k–ω model in the following two important flow situations of aerodynamic flows, viz., in an adverse pressure gradient boundary layer flow (typically on the upper side of an airfoil) and close to the stagnation point (at the leading edge of wing or fuselage).

4.1. Validation for adverse pressure gradient flow

In this section, we assess the range of validity of the boundary layer approximation (23) with $f = 0$ for two adverse pressure gradient (APG) flows. Firstly, we consider the flow over a flat plate at $Re = 4.1 \times 10^7$ devised by [8]. We use a flat plate of length $L = 8$ m with farfield data $u_\infty = 78\ \mathrm{m\,s^{-1}}$ and $\nu_\infty = 1.5 \times 10^{-5}\ \mathrm{m^2\,s^{-1}}$ At distance $y = 0.5$ m above the wall, suction and blowing is imposed by prescribing the wall-normal velocity component $v(x) = A\exp(-b(x - x_\alpha)^2) - A\exp(-b(x - x_\beta)^2)$ with $x_\alpha = 2.5$, $x_\beta = 5.5$, $A = 0.35x$, $b = 108/6^2$ which produces a streamwise pressure gradient leading to separation. Secondly, we study the flow around the "A-airfoil" (AS239) in highlift configuration for $Ma = 0.15$ at three different $Re = 2.0 \times 10^6$, 1.0×10^7, 4.0×10^7, and different angle of attack $\alpha = 10.2°$, 13,3°, 14,2°, 15.3°. We investigate the near-wall behaviour of the SA-E model and the SST k–ω model.

First we recall that for fixed APG, say fixed $\alpha = 13.3°$, p^+ is decreasing for increasing Re due to its definition, see Fig. 2 (left). As the separation point is approached, p^+ goes to infinity. Regarding the test cases under investigation, for the SA-E model, the region where (26) has universal (i.e., Re-number independent) solutions

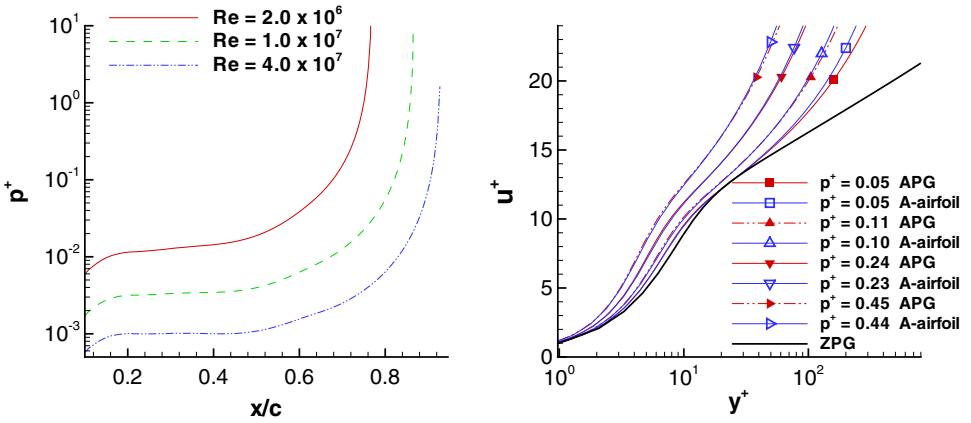

Fig. 2. Reynolds number dependence of p^+ (left) and universal p^+-dependent near-wall behaviour (right) for SA-E model.

depending only on the parameter p^+, is relatively large, see Fig. 2 (right). Therein, the A-airfoil for $\alpha = 13.3°$, $Re = 2 \times 10^6$ and the zero-pressure gradient flat plate solution (ZPG) are also shown.

Interestingly, SA-E and SST k–ω model show a different behaviour in APG flow. We focus on the flat plate APG flow, which has a p^+ behaviour close before separation similar to the A-airfoil at $Re = 4 \times 10^7$. We consider the velocity profiles $u^+(y^+)$ at different p^+-stations. The SST k–ω model shows a general breakdown of the universal ZPG solution, i.e., the character of the velocity profile changes over the entire buffer layer ($5 < y^+ < 50$) and log-layer ($y^+ > 50$), see Fig. 3. However, in the viscous sublayer ($y^+ < 5$) agreement with the universal ZPG solution is still very close, except at large p^+-values very close before separation.

On the other hand, the SA-E model shows a successive breakdown of the universal ZPG solution, i.e., the region occupied by the universal ZPG solution in reduced progressively, see Fig. 4 (left).

Now we consider the turbulence quantities. For the SA-E model, $\tilde{\nu}^+$ shows a much larger deviation from the universal ZPG solution than would be expected from the behaviour of the u^+-profiles, see Fig. 4 (right).

Fig. 5 shows the profiles for k^+ and ω^+. For ω a progressive reduction of the region of validity of the universal ZPG solution is observed. For k, a general breakdown of the ZPG solution in the *entire* near-wall region can be seen. This causes the general breakdown of the universal ZPG solution for u^+.

Finally, we study the profiles for eddy-viscosity. The deviation from the universal ZPG solution is large in the entire near wall region even for small p^+ and increasing rapidly with increasing p^+, see Fig. 6.

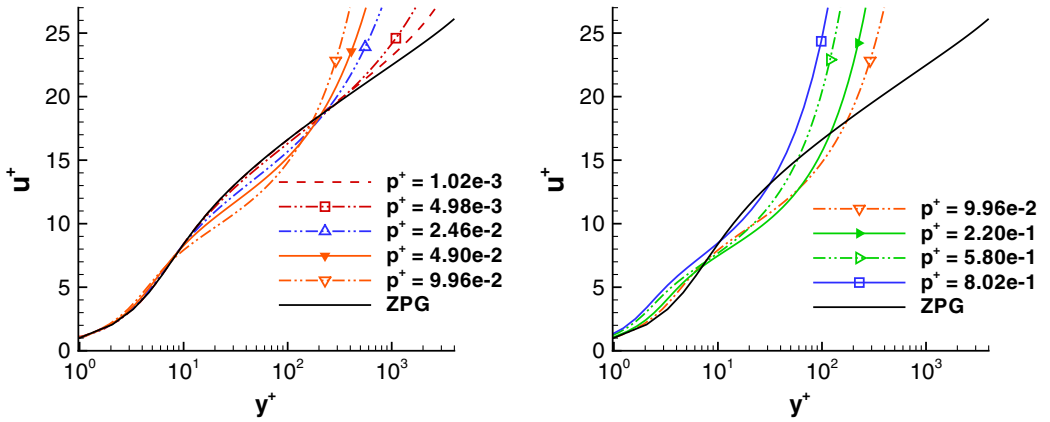

Fig. 3. Near-wall velocity profile for SST k–ω model at different p^+-stations for APG flow [8].

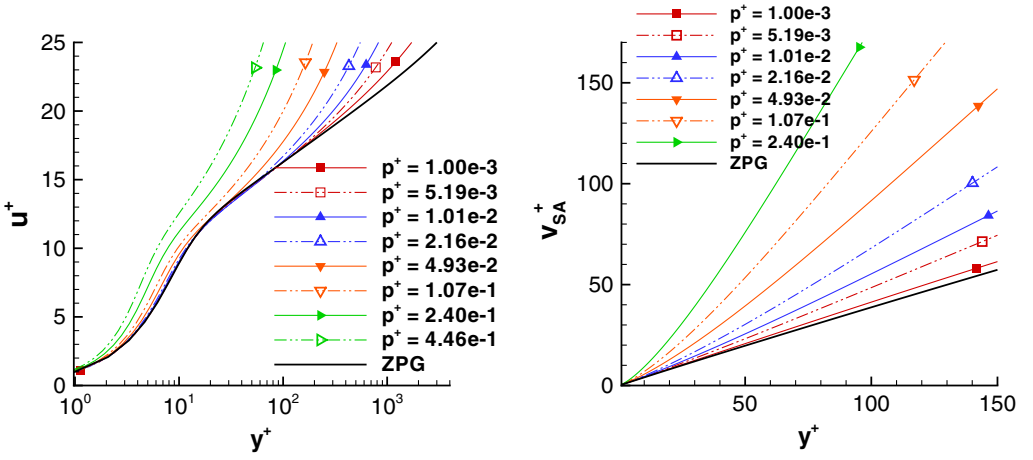

Fig. 4. u^+ and $\tilde{\nu}^+$ for SA-E model at different p^+-stations for the APG flow [8].

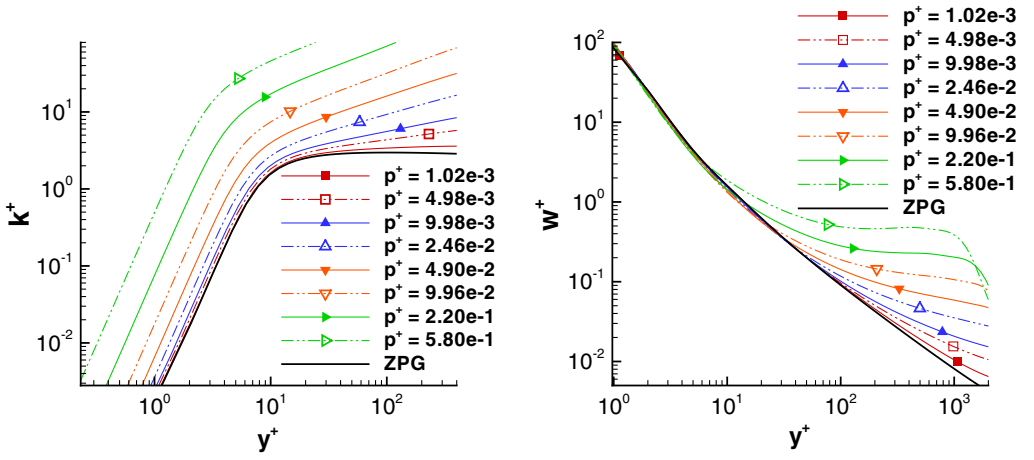

Fig. 5. Profiles for k^+ and ω^+ at different p^+-stations for APG flow [8].

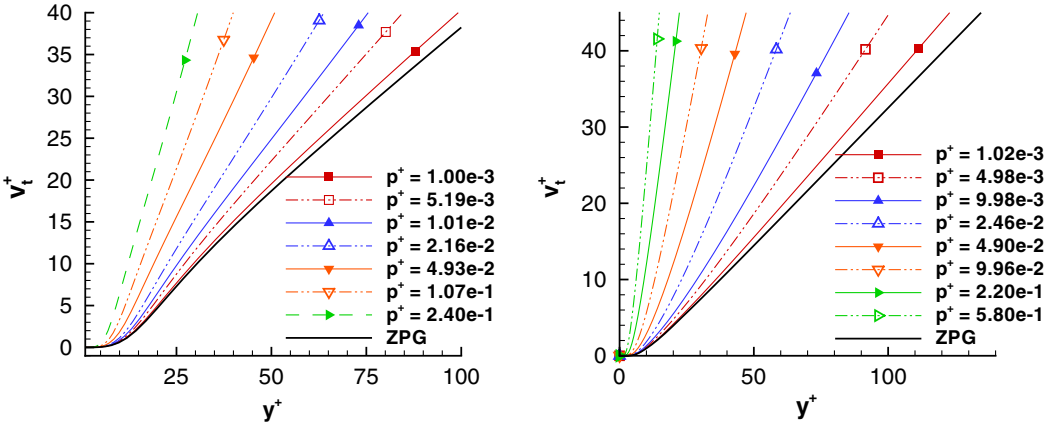

Fig. 6. Eddy viscosity for SA-E model (left) and SST k–ω model (right) for APG flow [8].

4.2. Near-wall behaviour of RANS solutions close to an airfoil leading edge

In this subsection, we study the near-wall behaviour of the SA-E and SST k–ω model close to the leading edge of the "A-airfoil" at $Ma = 0.15$, $Re = 2.0 \times 10^6$, and angle of attack $\alpha = 13.3°$. This flow is far from being fully turbulent due to the close distance to the stagnation point at $x/c = 0.03$ (with chord length c). Moreover, the flow is affected by the strong variation of p^+ together with the large mean-streamline curvature. Fig. 7 shows the p^+-distribution for two airfoil flows. Note that p^+ is positive for adverse pressure gradients and negative for favourable pressure gradients. Due to its definition, p^+ goes to infinity as the stagnation and separation points are approached.

We consider the solution at six stations $x_i = \xi_i c$ with $\xi_1 = 0.15$, $\xi_2 = 0.2$, $\xi_3 = 0.25$ on the lower side characterized by strong flow acceleration and $\xi_4 = 0.0003$, $\xi_5 = 0.0019$, $\xi_6 = 0.0044$ on the upper side, with corresponding p^+-values of order 10^{-2}. Regarding the velocity profiles, Fig. 8 shows that for $y^+ \lessapprox 10$, the agreement with the universal ZPG solution is very good for both SA-E and SST model. However, for the SA-E model, for increasing values of y^+, deviations from the ZPG solution become large.

The turbulence quantities are shown in Fig. 9. The profiles for ω are close to the universal ZPG-solution for $y^+ \lessapprox 30$. However, it is noteworthy that the near-wall solution for $\tilde{\nu}$ is far from its universal ZPG-profile.

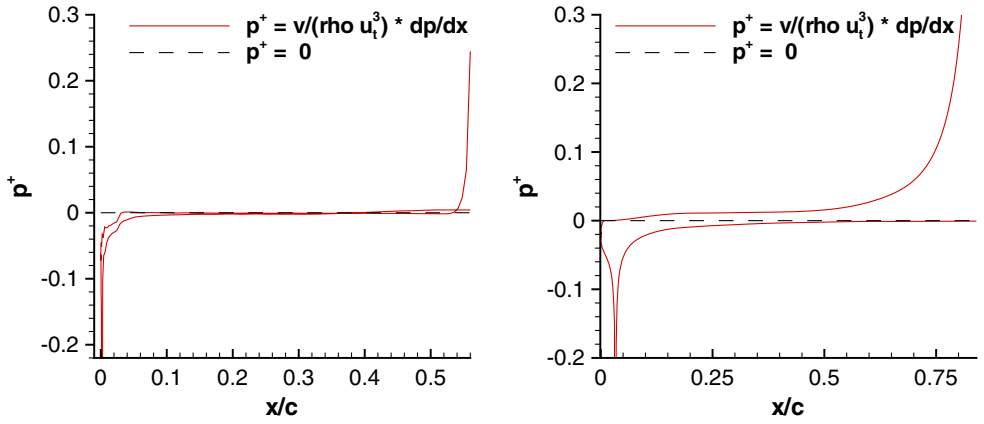

Fig. 7. Pressure gradient p^+ for RAE-2822 case 10 (left) and A-airfoil (right).

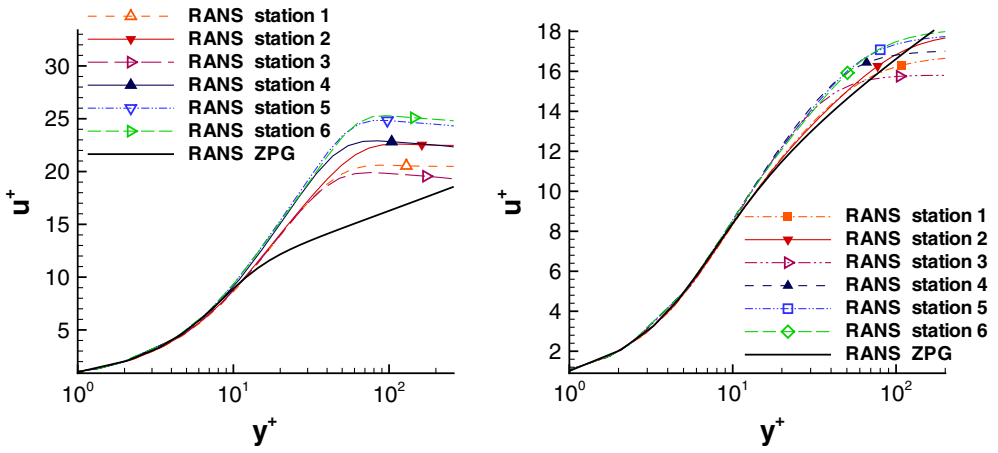

Fig. 8. Profiles of u^+ around the leading edge of A-airfoil for SA-E (left) and SST k–ω (right).

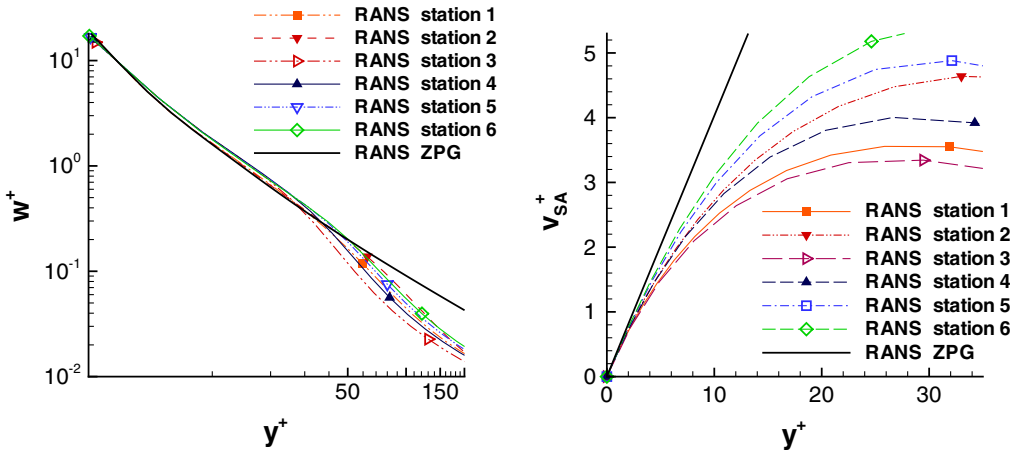

Fig. 9. Profile for ω for SST model and $\tilde{\nu}$ for SA-E model at leading edge of A-airfoil.

4.3. Implications for wall-functions and motivation for near-wall grid adaptation

In this subsection, we draw some implications for a suitable usage of universal wall-functions for non-equilibrium flows. In this paper, we are interested in flows with (i) stagnation points and subsequent not yet fully developed turbulent flow, (ii) regions of adverse pressure gradient with relatively large pressure gradient parameter, and (iii) regions of separation and reattachment.

The universal ZPG wall-functions for u and ω are still close to the RANS solution in the viscous sublayer even in regions (i) and (ii) provided p^+ is of at most moderate size. Moreover, it was shown in [8, p. 285], that in regions of separated flow and after reattachment the universal profiles are still close to the wall-resolved RANS solution in the viscous sublayer.

From Fig. 8 we infer that close to stagnation points, large first spacings $y^+(1)$ should be avoided, in particular for the SA model.

From Figs. 4–6 and 9 we see that the near-wall RANS solutions for k, $\tilde{\nu}$ and hence ν_t show large deviations from their universal ZPG profiles in situations (i) and (ii). Thus we may conclude that off-wall boundary conditions using the universal ZPG profile for k and $\tilde{\nu}$ are sources of grid-dependent solutions and should be avoided. Instead homogeneous Dirichlet conditions are recommended, see Section 7.

As suggested by Figs. 6 and 9 (right) we do not invoke $\nu_t^+ = \mathrm{d}y^+/\mathrm{d}u^+ - 1$, which is relation (26) with neglecting the p^+-term, as a consistency relation between u^+ and ν_t^+, because this may be an extra source of grid-dependence in non-equilibrium situations. The profiles of ν_t^+ change much larger than would be expected from the u^+-profiles, which is due to neglecting the p^+-term. Note that this is also supported by an a posteriori analysis. For this purpose, we integrated (26) numerically at different p^+ stations where the corresponding profile for ν_t^+ is taken from a spline interpolation of the RANS solution. Integration is performed with and without the p^+-term. Good agreement is found when the p^+-term is taken into account but poor otherwise.

Finally, we study the issue of large p^+-values close before separation. For large $Re \gtrapprox 10^7$, p^+ is small even close before separation and universal ZPG wall functions give almost grid independent results, as shown in [8, p. 284]. But for moderate Re-numbers, say $Re = 2 \times 10^6$ this term becomes important. With regard to the application of wall-functions, the fact that $u_\tau \to 0$ as separation is approached has two counteracting effects: The unfavourable effect is that close before separation p^+ becomes large such that the universal ZPG profiles for u and ω cease to be valid outside the viscous sublayer. The favourable point is that the thickness of the viscous sublayer in dimensional units is becoming larger, i.e., points at a given wall-distance located in the log-layer upstream of the separation point now may reside in the viscous sublayer.

The latter effect is illustrated in Fig. 10 (left). Therein, we consider two wall-parallel grid-lines and study their y^+ distribution on the upper side of the A-airfoil at $\alpha = 13.3°$. The grid-points initially reside in the log-layer. As the separation point is approached, their y^+-values move toward the viscous sublayer.

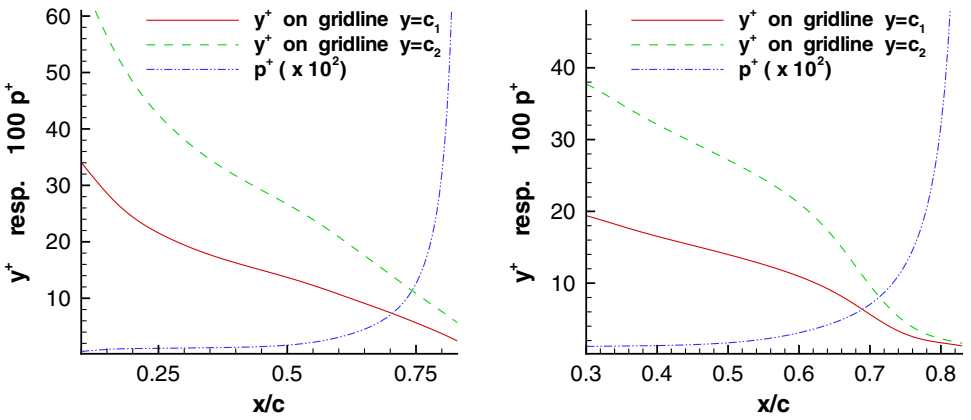

Fig. 10. Wall-distance in plus-units for two wall-parallel grid-lines in APG flow around A-airfoil without wall-normal grid adaptation (left) and with adaptation (right).

This effect can be enforced by applying a wall-normal grid adaptation which shifts the nodes closer to the wall, see Fig. 10 (right). Moreover, using such a grid adaptation, suitable values of $y^+(1)$ can be ensured also in flow regions (i) and (iii). This will be described in detail in Section 6.

5. Turbulence model consistent universal wall functions

In boundary layer flows at ZPG, the condition on turbulence model consistency $\nu_t^{bl} = \nu_t$ implies that model specific wall-functions are required. As the near-wall profiles of different versions of the Spalart–Allmaras model resp. the k–ω model almost collaps [21], it is sufficient to specify one model-consistent universal wall-function for the Spalart–Allmaras model, denoted F_{SA}, and one for the k–ω model, referred to as $F_{k\omega}$.

$$F_{SA} = (1-\phi_{SA})F_{Sp,5} + \phi_{SA}F_{Rei,m}, \quad \phi_{SA} = \tanh(\arg^3), \quad \arg = y^+/24, \tag{27}$$

$$F_{k\omega} = (1-\phi_{k\omega})F_{Sp,3} + \phi_{k\omega}F_{Rei,m}, \quad \phi_{k\omega} = \tanh(\arg^2), \quad \arg = y^+/50, \tag{28}$$

which are plotted in Fig. 11. Therein, we use Reichardt's law of the wall

$$u^+ = F_{Rei}(y^+), \quad F_{Rei}(y^+) \equiv \frac{\ln(1+0.4y^+)}{\kappa} + 7.8\left(1 - e^{-\frac{y^+}{11.0}} - \frac{y^+}{11.0}e^{-\frac{y^+}{3.0}}\right) \tag{29}$$

with $\kappa = 0.41$. We apply the following blending with the classical log-law $F_{log} = \ln(y^+)/\kappa + 5.1$, viz.,

$$F_{Rei,m} = (1-\phi_{bl})F_{Rei} + \phi_{bl}F_{log}, \quad \phi_{bl} = \tanh(\arg^4), \quad \arg = y^+/27. \tag{30}$$

Spaldings law [22] with parameter $N \in \{3,4,5\}$ is given by the inverse formula

$$y^+ = F_{Sp,N}^{-1}(u^+), \quad F_{Sp,N}^{-1}(u^+) \equiv u^+ + e^{-\kappa 5.2}\left(e^{\kappa u^+} - \sum_{n=0}^{N}\frac{(\kappa u^+)^n}{n!}\right). \tag{31}$$

Of crucial importance is the near-wall solution for ω. Instead of the standard blending [7], a new proposal avoids the deviation of ω from its low-Re solution in the buffer layer, viz.,

$$\text{Standard blending}: \omega = \sqrt{\omega_{vis}^2 + \omega_{log}^2}, \tag{32}$$

$$\text{New proposal}: \omega = \phi\omega_{bl} + (1-\phi)\omega_{b2}, \quad \phi = \tanh(\arg^4), \quad \arg = \frac{y^+}{10} \tag{33}$$

with the following blending formula and the asymptotic relations

$$\omega_{bl} = \omega_{vis} + \omega_{log}, \quad \omega_{b2} = \left(\omega_{vis}^{1.2} + \omega_{log}^{1.2}\right)^{1/1.2}, \quad \omega_{vis} = \frac{6\nu}{\beta_\omega y^2}, \quad \omega_{log} = \frac{u_\tau}{\sqrt{\beta_k}\kappa y}. \tag{34}$$

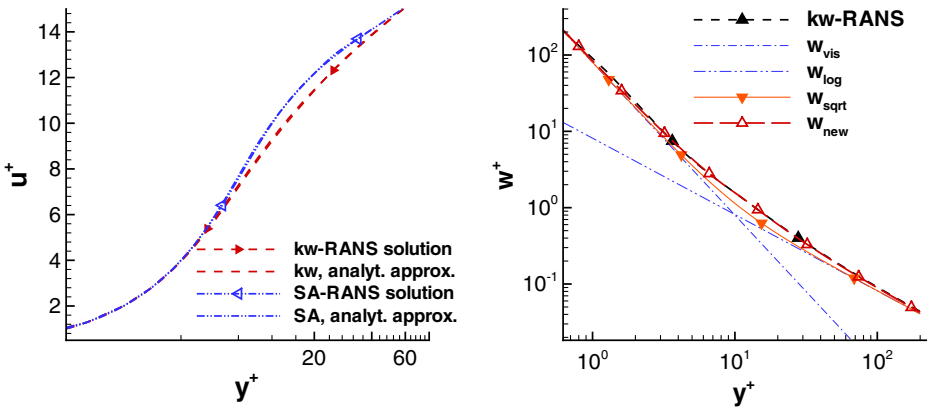

Fig. 11. New wall-functions for SA- resp. k–ω type models (left), wall law for ω (right).

In [8] a cubic spline interpolation of the near-wall RANS solution instead of closed formula is used. However, the aim of the present approach is to also allow for an easy dissemination of the method to other CFD codes.

5.1. Iterative solution strategy

Suppose a solution of (23) with $f = 0$ is known in either of the two closed forms

$$u^+ = F(y^+) \Longleftrightarrow \frac{u}{u_\tau} = F\left(\frac{yu_\tau}{\nu}\right) \quad \text{or} \quad y^+ = F^{-1}(u^+) \Longleftrightarrow \frac{yu_\tau}{\nu} = F^{-1}\left(\frac{u}{u_\tau}\right) \tag{35}$$

then the matching condition $u^{\mathrm{bl}} = u_\delta$ on Γ_δ and the relation $u^{\mathrm{bl}} = u_\tau F(yu_\tau/\nu)$ imply

$$F\left(\frac{y_\delta u_\tau}{\nu}\right) = \frac{u_\delta}{u_\tau} \quad \text{resp.} \quad F^{-1}\left(\frac{u_\delta}{u_\tau}\right) = \frac{y_\delta u_\tau}{\nu} \tag{36}$$

which can be solved for u_τ using Newton's method.

Remark 1. Newton's method for the direct form $u^+ = F(y^+)$ requires about three to four iteration steps independent of y^+. For the inverse formula $y^+ = F^{-1}(u^+)$ convergence problems can be observed for $y^+(1) \gtrapprox 300$ since Newton's method for the inverse formula is ill-conditioned. Thus the direct formulation should be used for large y^+-values.

Denote $\mathrm{TM} \in \{\mathrm{SA}, k\omega\}$ and $N \in \{3, 5\}$. For the numerical solution of

$$\frac{u_\delta}{u_\tau} = F_{\mathrm{TM}}\left(\frac{y_\delta u_\tau}{\nu}\right), \quad F_{\mathrm{TM}} = (1 - \phi_{\mathrm{TM}})F_{\mathrm{Sp,N}} + \phi_{\mathrm{TM}}F_{\mathrm{Rei,m}}$$

we proceed as follows:

(1) From the initial guess $u_\tau^0 = u_\delta/y_\delta$, seek $u_{\tau,\mathrm{Rei}}$ as solution of $u_\delta/u_\tau = F_{\mathrm{Rei,m}}(y_\delta u_\tau/\nu)$.
(2) Using the initial guess $u_\tau^0 = u_{\tau,\mathrm{Rei}}$, seek $u_{\tau,\mathrm{Sp}}$ as solution of $y_\delta u_\tau/\nu = F_{\mathrm{Sp,N}}^{-1}(u_\delta/u_\tau)$.
(3) Compute ϕ_{TM} and set $u_\tau = (1 - \phi_{\mathrm{TM}})u_{\tau,\mathrm{Sp}} + \phi_{\mathrm{TM}}u_{\tau,\mathrm{Rei}}$.

In our experience, steps (1) and (2) require each three to four iteration steps for convergence. The global hybrid-Re problem (8)–(16) with the wall function model (36) is solved iteratively until convergence is reached. Given an initial global flow solution, we can compute $\tau_{\mathrm{w}} = \rho u_\tau^2$ from (36). This provides the boundary condition on Γ_{w}, and the new global flow solution can be computed.

6. Wall-normal grid adaptation

We may conclude from Section 4 that in the following flow situations the deviation of the universal ZPG solution from the low-Re RANS solution is becoming large as y^+ is increased: (a) stagnation points with subsequent not fully developed flow, (b) strong pressure gradients ($p^+ \gtrapprox 0.05$), and (c) regions of separated flow. We point out that even if the pressure gradient parameter would be taken into the wall-function method such that grid independent results for pressure induced separation could be obtained, the problems near the leading edge and in regions of separated and reattached flow would still limit application to complex aerodynamic flows. Grid-adaptation is a solution strategy for all situations (a)–(c).

Thus, as a remedy, a *near-wall grid adaptation* [23] is employed. We assume that inside the prismatic layer, the nodes are located on rays starting at the corresponding wall node. We use the following notation, see Fig. 12 (left):

- $\vec{x}_{\mathrm{wp}}$: surface (wall) node,
- $\vec{x}_{\mathrm{np}}$: first node above the wall corresponding to node wp,
- $\{\vec{x}_{\mathrm{wp}} + \lambda_p\vec{r}\}$: ray of points starting at wall node $\vec{x}_{\mathrm{wp}}$ and ending at the tetrahedral layer; $\{\vec{x}_{\mathrm{wp}} + \lambda_p\vec{r}\} \equiv \{\vec{x} \in \mathbb{R}^d | \vec{x} = \vec{x}_{\mathrm{wp}} + \lambda_p\vec{r},\ 0 \leqslant p \leqslant p_{\max}\}$, where the direction vector $\vec{r}$ may be non-constant.

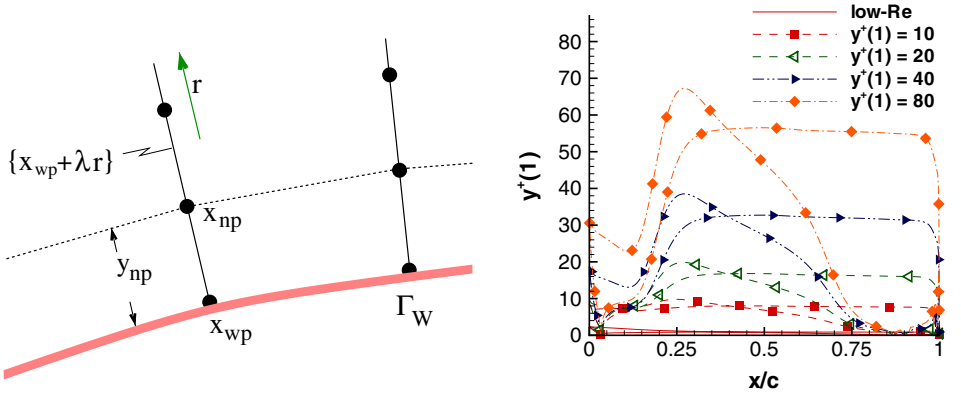

Fig. 12. Left: Notation for near-wall grid adaptation. Right: $y^+(1)$ for A-airfoil on adapted grid.

Moreover, we assume that $\vec{x}_{\mathrm{np}} - \vec{x}_{\mathrm{wp}}$ is almost parallel to the surface normal vector $\vec{n}$. Then the algorithm for y^+-adaptation may be written as follows:

(1) Read RANS solution and grid.
(2) y^+ grid adaptation.
  (a) For each surface node $\vec{x}_{\mathrm{wp}}$ do:
    (i) Determine $\vec{x}_{\mathrm{np}}$.
    (ii) Calculate u_τ using (29). From the wall-distance $y_{\mathrm{np}} = |\vec{x}_{\mathrm{np}} - \vec{x}_{\mathrm{wp}}|$ determine the wall-distance in plus units y^+_{np}.
    (iii) Check if $\vec{x}_{\mathrm{wp}}$ is located in a region of flow stagnation and strong surface curvature.
    (iv) Determine p^+ from (25) and check if $|p^+| > p^+_0$ for a given threshold p^+_0.
    (v) Check if point $\vec{x}_{\mathrm{wp}}$ resides in a separation region.
    (vi) Based on (2a.iii)–(2a.v) set target value y^+_{target}.
    (vii) If $y^+_{\mathrm{target}} < y^+_{\mathrm{np}}$ then set $y_{\mathrm{new}} = y_{\mathrm{np}} y^+_{\mathrm{target}}/y^+_{\mathrm{np}}$, else $y_{\mathrm{new}} = y_{\mathrm{np}}$.
  (b) Smooth the y_{new}-distribution.
  (c) For each surface node redistribute the points on its ray $\{\vec{x}_{\mathrm{wp}} + \lambda_p \vec{r}\}$ where the last point $\vec{x}_{\mathrm{wp}} + \lambda_{\mathrm{p,max}}\vec{r}$ remains unchanged.
(3) Interpolate RANS solution from old grid to new grid.

Some technical details are described in the following. Calculating u_τ using (29) is sufficient for the adaptation. We use the threshold value $p^+_0 = 0.09$ for indicating regions of strong pressure gradient. Concerning the target value for y^+, numerical tests suggest $y^+_{\mathrm{target}} \in [5, 10]$ in regions of flow stagnation and strong surface curvature and $y^+_{\mathrm{target}} \in [1, 5]$ in regions of separation.

Smoothing of the y_{new}-distribution is performed as follows. Denote K the number of smoothing steps, $y^i_{\mathrm{np}} = y_{\mathrm{new}}$ of node $\vec{x}^i_{\mathrm{np}}$ after (2a.vii), $\mathcal{N}(i)$ the set of indices of neighbour (adjacent) surface nodes of node i and $\#\mathcal{N}(i)$ their number. Then in smoothing step k

$$y^{i,k}_{\mathrm{np}} = (1-\epsilon) y^{i,k-1}_{\mathrm{np}} + \epsilon y^{\mathrm{nei},k-1}_{\mathrm{np}} \quad \text{with } y^{\mathrm{nei},k-1}_{\mathrm{np}} = \frac{1}{\#\mathcal{N}(i)} \sum_{j \in \mathcal{N}(i)} y^{j,k-1}_{\mathrm{np}}.$$

The wall-normal grid adaptation can also be used to increase $y^+(1)$ in regions of attached boundary layer flow close to equilibrium, where p^+ is small and almost constant. A typical area of application is the fuselage of an airfoil. This can be used to accelerate the convergence of the flow solver.

7. Discretization using an explicit finite volume method

Computations are performed using the DLR TAU-code, which is of cell-vertex type, i.e., of cell-centered type w.r.t. the dual grid cells. The convective fluxes are calculated by a central scheme with artificial scalar

dissipation [24]. The gradients of the flow variables are reconstructed using a Green–Gauss–MUSCL formula. The arising fixed-point problem is iterated in fictitious pseudo-time using a low-storage k-stage Runge–Kutta scheme by Jameson [25].

In the present method, boundary cells are half cells in the sense that the corresponding grid nodes are located on the boundary. This allows to impose homogeneous Dirichlet boundary conditions for k and $\tilde{\nu}$. Concerning the hybrid wall-function boundary condition, the standard approach for cell-centered type FVM to simply modify μ_t in the boundary cell (see [22] Eqs. (9a) and (10a)) cannot be used. Therefore, the fluxes across the wall are prescribed using (11), (13) with the approximative relation

$$\mathbb{T}\cdot\vec{n} = (\mathbb{I} - \vec{n}\otimes\vec{n})\mathbb{T}\cdot\vec{n} + \vec{n}\otimes\vec{n}\mathbb{T}\cdot\vec{n} \approx -\tau_w\vec{u}_t,$$

where the normal contribution of the wall-shear stress is neglected.

The global hybrid-Re problem (8)–(16) with the wall function model (36) is solved iteratively in pseudo time until convergence is reached.

8. Numerical results

8.1. Flat plate turbulent boundary layer with zero pressure gradient

The ability of the wall function proposal described in Section 5 to give solutions almost independent of the wall-normal grid spacing in zero-pressure gradient flows is demonstrated. We consider the turbulent boundary layer flow at zero pressure gradient over a flat plate of length $l = 5$ m studied experimentally by Wieghardt and recorded in [26] as Flow 1400. In agreement with the experimental setup we use $u_\infty = 33$ m/s, $\nu = 1.51\times 10^{-5}$ m^2/s and an adiabatic wall. Transition from laminar to turbulent flow is prescribed in agreement with the formula for the critical Reynolds number where transition occurs (cf. [27, p. 471]).

The grid-dependence using the classical wall laws (31) and (29) is shown in Fig. 13 (left) by plotting the relative error in skin friction $c_f = \tau_w/(0.5\rho_\infty u_\infty^2)$ in the interval $2 \leqslant x \leqslant 4.5$ between the low-Re solution $c_f^{\text{l.R.}}$ and the solution with wall-functions $c_f^{\text{w.f.}}$ for the SA–Edwards model, where $y^+(1)$ denotes the wall distance of the first node above the wall in viscous units.

Figs. 13 (right) and 14 show the almost grid independent results for the new wall functions. In order to obtain grid independent results for k–ω type models, it is crucial to use (7) and (33) for the ω boundary condition.

As a final remark, method (28), (7), (33) gives almost grid-independent predictions for all versions of the k–ω model considered, including non-linear variants and explicit algebraic Reynolds-stress models, see Fig. 15. The variation in c_f due to a variation in $y^+(1)$ is significantly smaller than the different predictions among the various k–ω model versions.

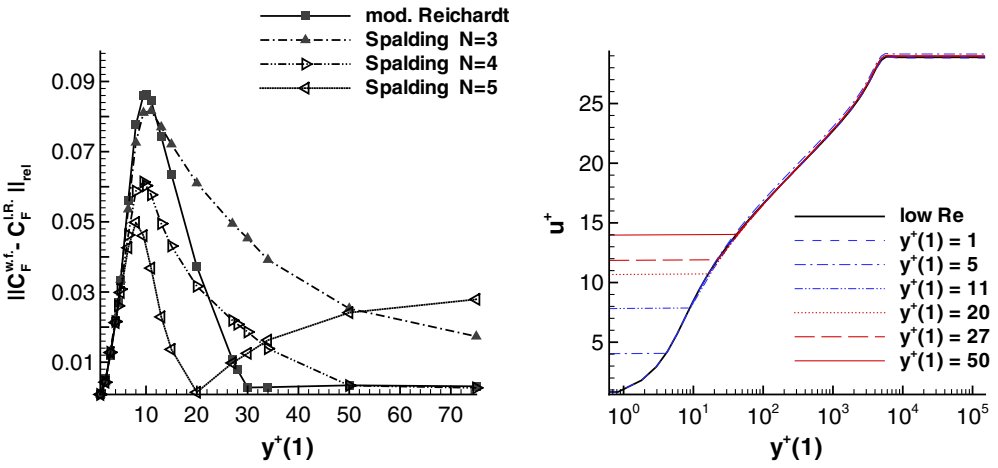

Fig. 13. Grid-dependence of classical wall-functions (left), new velocity results for k–ω model (right).

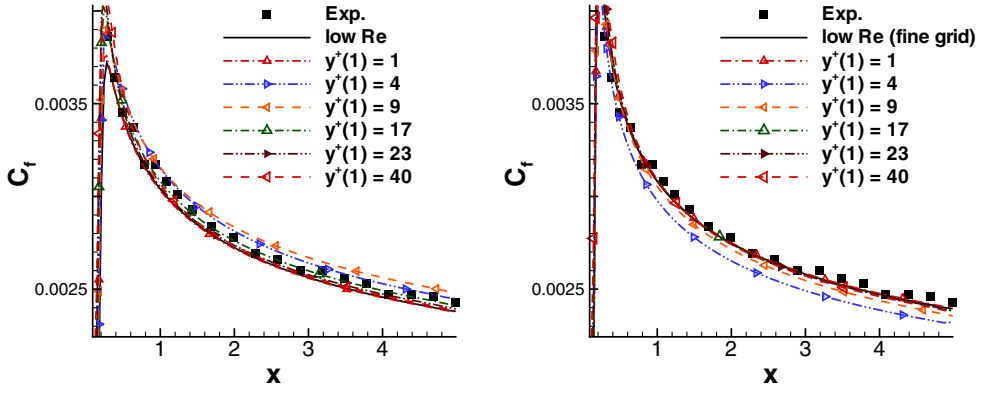

Fig. 14. Prediction of c_f for SA-E model (left) and for baseline k–ω model [15] (right).

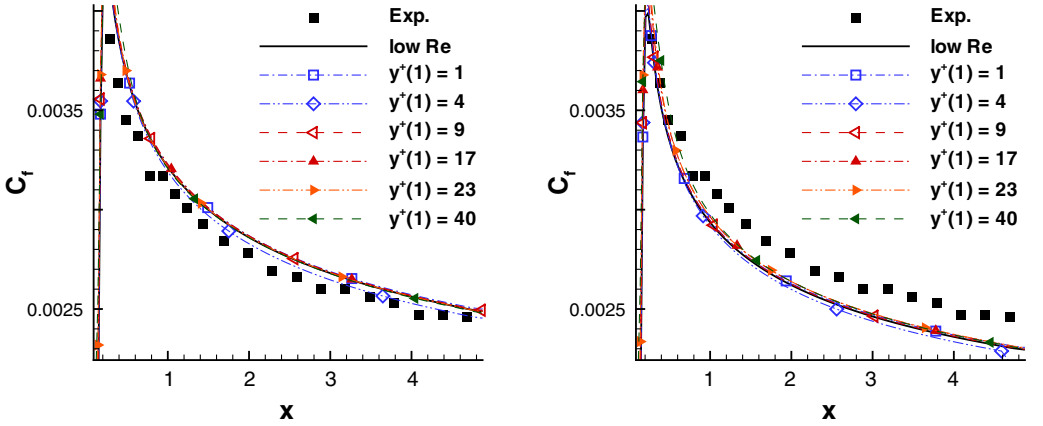

Fig. 15. Application to EARSM k–ω models [17] (left) and [18] (right).

8.2. Transonic airfoil flows RAE-2822 cases 9 and 10

In this section, we apply the method to the transonic airfoil flows RAE-2822 case 9 (no/small separation region at $Ma = 0.73$, $Re = 6.5 \times 10^6$ and angle of attack $\alpha = 2.8°$) and case 10 (shock induced separation at $Ma = 0.75$, $Re = 6.2 \times 10^6$ and $\alpha = 2.8°$) investigated experimentally in [28]. We consider a series of hybrid-Re grids of O-type with $y^+(1)$ varying from 1 to 60, generated using the commercial grid generation tool CentaurSoft (*www.centaursoft.com*). Fig. 16 shows the $y^+(1)$-distribution for the SST k–ω model. The grids are built such that the thickness of the prismatic layer has an almost constant value around $0.052c$ (with chord length c) which fully contains the boundary layer. It is worthwhile pointing out that the generation of grids with $y^+(1) \gtrapprox 8$ is much simpler than for low-Re grids.

We consider the predictions for the pressure coefficient c_p and the local skin friction coefficient $c_f^{(\mathrm{loc})}$ (based on the local dynamic pressure at the boundary layer edge q_P, [28]). Preliminary calculations show that prescribing transition at $x/c = 0.03$ according to the experiment or treating the wall as fully turbulent has only a small influence which is restricted to the region $x/c \leqslant 0.05$.

8.2.1. Transonic airfoil flow RAE-2822 case 10

The results for the SA-E model are given in Figs. 17 and 18. The agreement in c_p on the various grids is very good. On the coarser grids with $y^+(1) \gtrapprox 40$, around the leading edge the deviation is small in c_p but discernible in c_f. On the upper side in the fully turbulent region before the shock ($x/c \lessapprox 0.5$), the behaviour in c_f is similar to the flow over a flat plate: The predictions for $y^+(1) = 1$ and $y^+(1) \gtrapprox 20$ almost collapse whereas

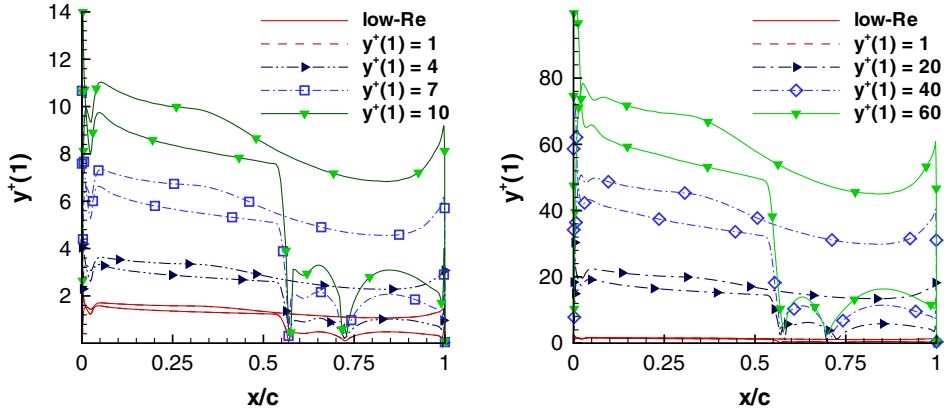

Fig. 16. RAE case 10: Distribution of $y^+(1)$ for SST k–ω model [15].

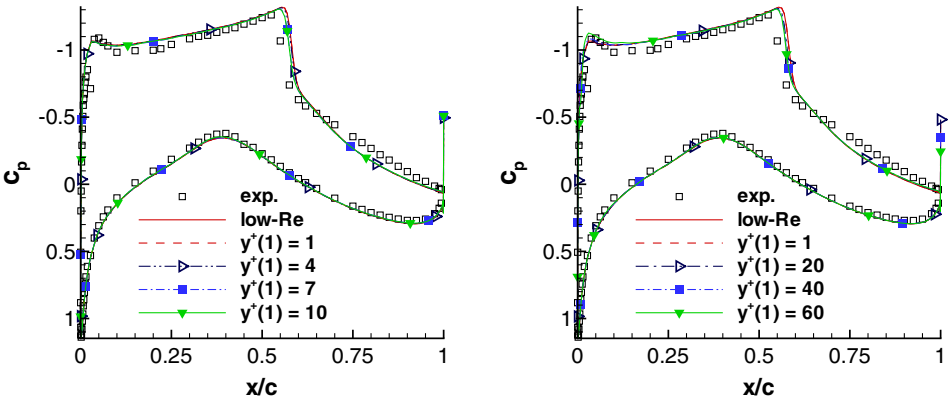

Fig. 17. RAE case 10: Distribution of c_p for the SA-E model.

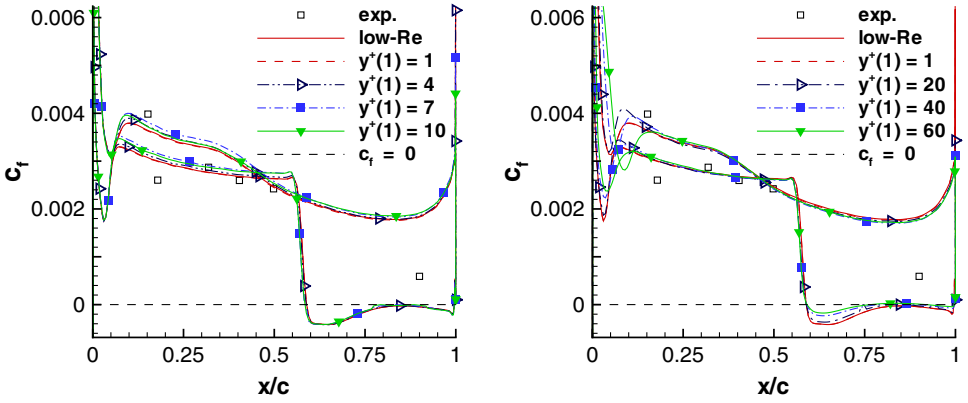

Fig. 18. RAE case 10: Distribution of c_f for the SA-E model.

in the intermediate region of $y^+(1)$ the deviation is slightly larger. In the separation region, the agreement on intermediate-Re grids with $y^+(1) \lessapprox 10$ is surprisingly good, whereas on the coarser grids $y^+(1) \gtrapprox 20$ the differences become larger.

The results for the SST k–ω model are plotted in Figs. 19 and 20. We mention that (7) is superior to (6) in giving grid-independent results for high-Re grids $y^+(1) \gtrapprox 40$, whereas for $y^+(1) \lessapprox 10$ both boundary condi-

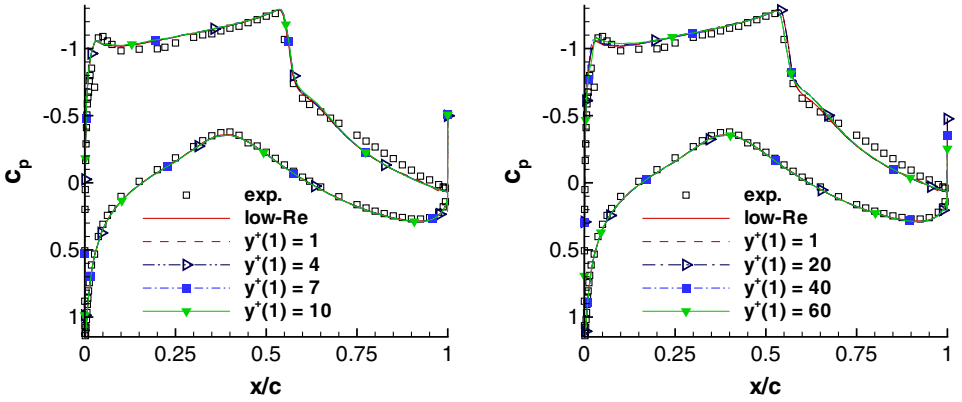

Fig. 19. RAE case 10: Distribution of c_p for SST k–ω model with Wilcox b.c.

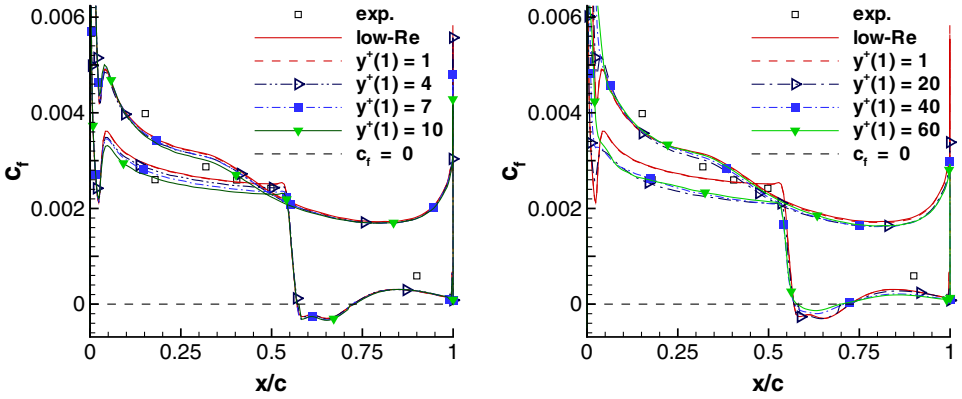

Fig. 20. RAE case 10: Prediction of c_f for SST k–ω model with Wilcox b.c.

tions are almost equal. The deviations around the leading edge are similar to the SA-E model. In the fully turbulent region on the upper side before the shock, there are moderate deviations in c_f on the intermediate-Re and high-Re grids.

8.2.2. Transonic airfoil flow RAE-2822 case 9

For case 9, the SA-E model predicts a slight shock-induced separation for the low-Re b.c. and for $y^+(1) \lessapprox 20$ (with hybrid-Re b.c.), whereas for $y^+(1) \gtrapprox 40$ no shock-induced separation is predicted, see Fig. 21. In all cases, the flow remains attached near the trailing edge. It should be noted that on a similar low-Re grid of H-type, after reattachment a slight trailing edge separation is predicted. This stresses the influence of the grid topology on the results.

Regarding the SST k–ω model, on all grids except for $y^+(1) = 60$ a slight shock induced separation is predicted in agreement with the low-Re result, see Fig. 22. In all cases the flow remains attached near the trailing edge.

8.3. Subsonic A-airfoil in highlift configuration

In this section, we apply the wall-function method to the subsonic flow around the "A-airfoil" (AS239) in highlift configuration at $Ma = 0.15$, $Re = 2.0 \times 10^6$, and angle of attack $\alpha = 13.3°$, studied experimentally in [29,30]. The strong adverse pressure gradient on the upper side causes the turbulent boundary layer to separate close to the trailing edge. In the experiment, transition was prescribed at $x/c = 0.3$ on the lower side and free transition was observed at $x/c = 0.12$ on the upper side.

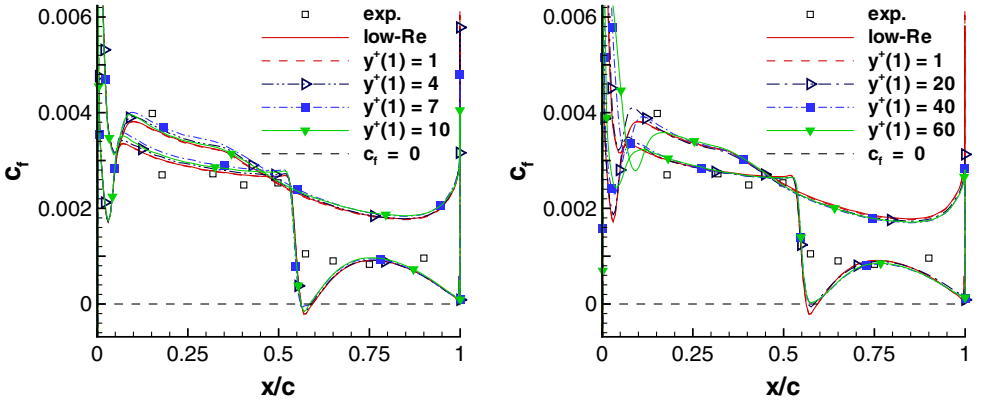

Fig. 21. RAE case 9: Distribution of c_f for the SA-E model.

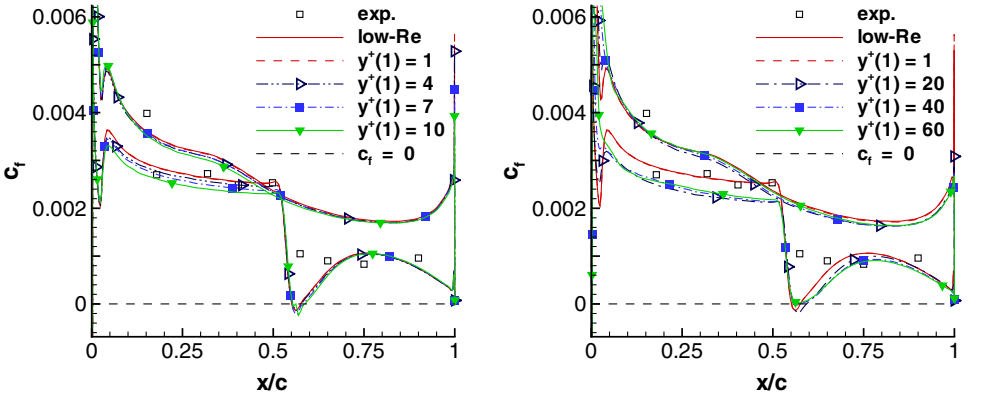

Fig. 22. RAE case 9: Distribution of c_f for the SST k–ω model with Wilcox b.c.

However, in the present computations the airfoil surface is treated fully turbulent. The laminar boundary layer region is relatively large for the A-airfoil in the experiment and the present wall-function model relies on a fully-turbulent boundary-layer relation for the wall-shear stress. As the focus is on grid-independence of the wall-function method, the question of laminar-turbulent transition modelling is not considered here. Note that neglecting transition increases the deviation from the experimental data significantly.

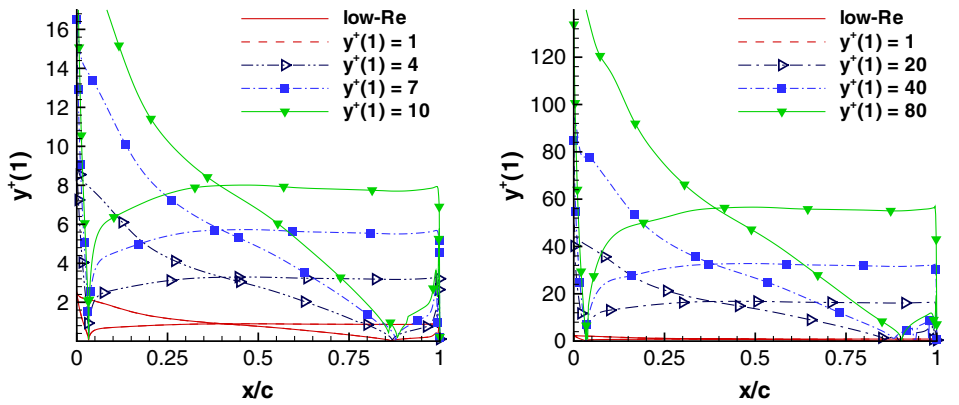

Fig. 23. A-airfoil: Distribution of $y^+(1)$ for the SST k–ω model.

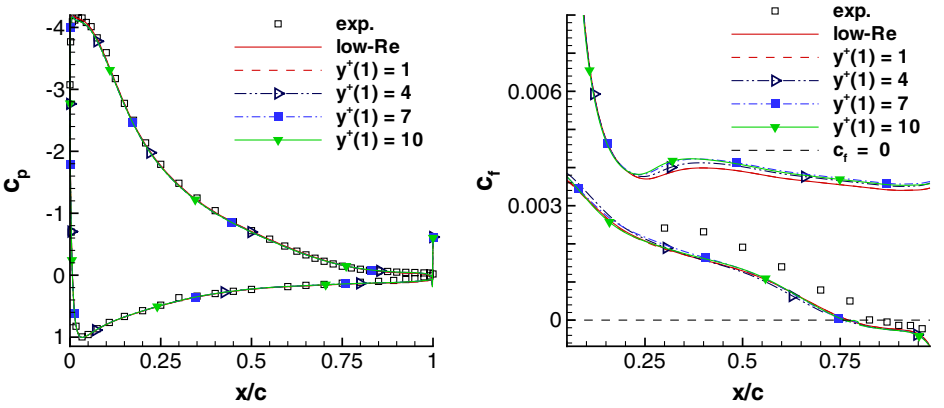

Fig. 24. A-airfoil: Prediction for c_p (left) and c_f (right) for SA-E model.

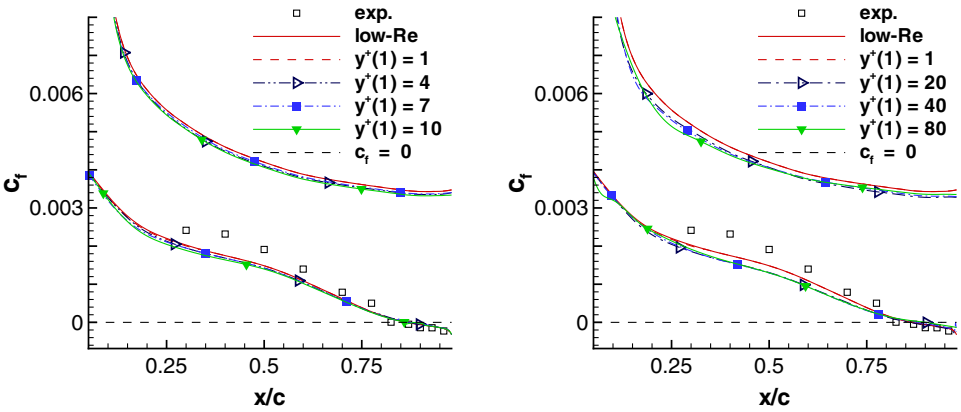

Fig. 25. A-airfoil: Prediction for c_f for SST k–ω model with Wilcox b.c. (7).

The O-type grids with their $y^+(1)$-distribution are shown in Fig. 23, where the denoting value has to be seen as an average over the chord length. This test case is very interesting and challenging for wall-functions, as $y^+(1)$ ceases from its maximal value near the leading edge to zero at the separation point.

The results for the SA-E model on the grids with $y^+(1) \leqslant 10$ are shown in Fig. 24 and show close agreement with the low-Re solution. The two solutions with $y^+(1) = 40$ and $y^+(1) = 80$ suffer from local oscillations in c_p near the leading edge and are not shown here. This can be remedied by ensuring smaller values for $y^+(1)$ near the leading edge (e.g., by using a grid adaptation) or by using a modified boundary condition for $\tilde{\nu}$. Regarding the latter, we can prescribe $\tilde{\nu} = \tilde{\nu}_{cs}$ on Γ_δ, where $\tilde{\nu}_{cs}$ is the spline interpolation of the universal near-wall solution for $\tilde{\nu}$ [8], but then results become inferior on intermediate-Re grids, see [21].

For the SST k–ω model with Wilcox b.c. (7) (see Fig. 25), on all grids the agreement in c_f with the low-Re solution is remarkably good, in particular for $y^+(1) \lessapprox 10$. We remark that the results for the SST k–ω model with boundary condition (6) show a discernible underprediction for c_f on the high-Re grids, see [21].

9. Combination of wall-normal grid adaptation and wall-functions

In this section, we apply the grid-adaptation technique described in Section 6 to the two test cases considered in the previous section. For the A-airfoil we use $\epsilon = 0.6$ and $K = 200$. Fig. 12 (right) shows the y^+-distribution on the adapted grids. Fig. 26 shows that the grid-independence of the c_f-distribution is improved noticeably.

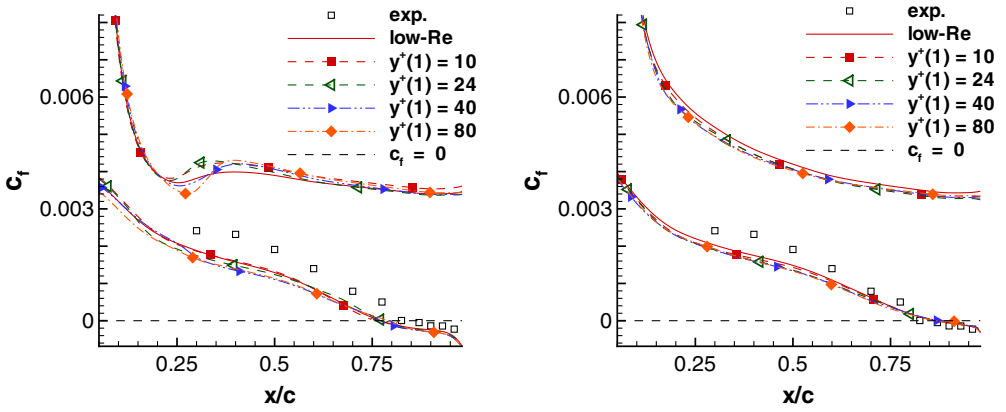

Fig. 26. A-airfoil: c_f after y^+-adaptation for SAE (left) and SST k–ω (right).

For the SA-E model, near-wall grid adaptation around the leading edge is necessary for ensuring stability of the method on the high-Re grids, as for large y^+-values the velocity profiles are too far from the universal ZPG solution, recall Fig. 8. Further tests show that limiting $y^+(1)$, e.g., $y^+(1) \lessapprox 50$ around the leading edge is sufficient to ensure stability, i.e., to avoid oscillations. This can be the method of choice if large $y^+(1)$-values are desired in order to obtain a large convergence acceleration.

Table 1 gives the separation point without and with y^+-adaptation. Therein N_y denotes the number of wall normal nodes in the prismatic layer. Values denoted by $(\,)^*$ indicate that the solution suffers from strong oscillations near the leading edge.

Table 1
Prediction of separation point for A-airfoil without and with $y^+(1)$ adaptation

$y^+(1)$ (average)	N_y	x_{sep}/c SA-E	x_{sep}/c SA-E (y^+-adap)	x_{sep}/c SST k–ω	x_{sep}/c SST k–ω (y^+-adap)
Low-Re	33	0.771	–	0.866	–
1	33	0.770	–	0.866	–
4	28	0.755	–	0.863	–
7	26	0.759	–	0.868	–
10	24	0.761	–	0.861	–
20	21	0.787	0.776	0.861	0.864
40	19	(0.838)*	0.771	0.881	0.873
80	17	(0.881)*	0.788	0.903	0.867

Values denoted by $(\,)^*$ suffer from local oscillations at the leading edge.

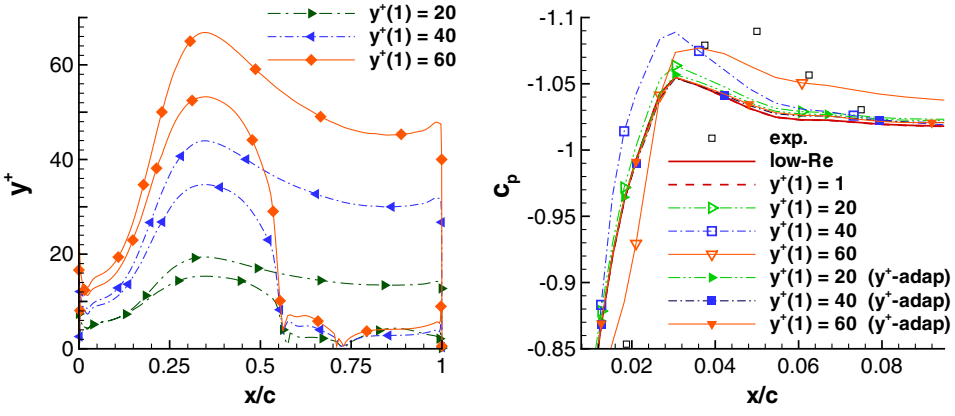

Fig. 27. RAE case 10 on adapted grid: $y^+(1)$ (left) and detail of c_p for SST k–ω (right).

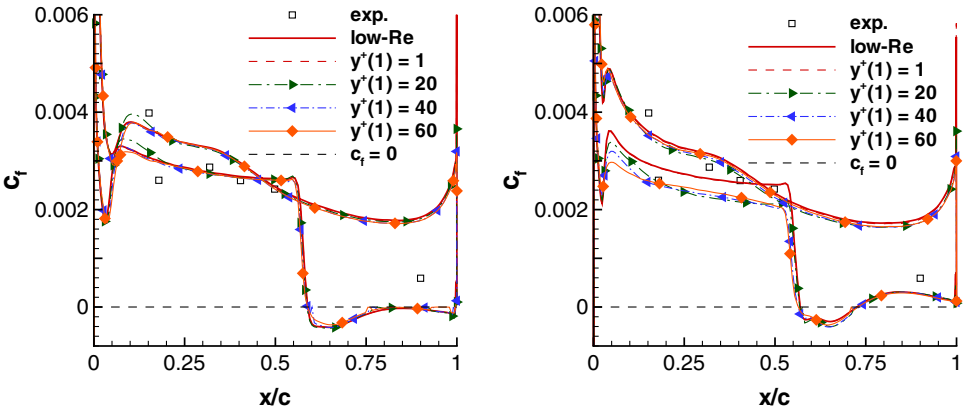

Fig. 28. RAE case 10 on adapted grid for SA-E (left) and SST k–ω (right).

The SST k–ω model predicts a too late separation point on the high-Re meshes without near-wall adaptation. This stems from the influence of significant p^+-values on the near-wall velocity profile over a relatively large streamwise distance due to the moderate Reynolds-number, recall Figs. 3 and 10.

Finally, it is worthwhile pointing out that the grid-dependence is much smaller than the spreading due to the uncertainty associated with the turbulence model.

Secondly, we apply the approach to the RAE 2822 case 10. Here we are interested in a better resolution of the leading edge and the aft-shock separation region. Both regions are critical to obtain correct moments e.g. for aeroelastic applications. Fig. 27 (left) shows that the wall-normal grid is shifted towards the low-Re regime in the vicinity of the leading edge, close to the shock and in the separation region. The improvement of grid-independence in c_p (Fig. 27 (right)) and in c_f in the separation region (Fig. 28) is discernible. In particular, the prediction for the reattachment point is almost grid-independent.

10. Conclusions

A new grid and flow adaptive wall-function strategy has been presented. This strategy consists of two parts, namely, a hybrid wall-function proposal suitable for non-equilibrium flows and a near-wall grid adaptation method with a flow-based sensor.

Based on an investigation of the near-wall behaviour of the SA-E and the SST k–ω model in non-equilibrium flow situations, improvements of the wall-function method for applications to aerodynamic flows are suggested, most notably to avoid off-wall boundary conditions for turbulent kinetic energy and eddy viscosity using their universal equilibrium solutions.

A new combination of wall-functions and near-wall grid adaptation ensures both an appropriate resolution of near-wall flow physics and takes into account the range of validity and stability of the wall-function model.

The treatment of laminar flow regions and the question of transition from laminar to turbulent flow is subject of future research. Moreover, future work will focus on applications to unsteady flow problems. It is also intended to apply this method as a new near-wall model for large-eddy simulation and to a new class of so-called scale adaptive models [31], which are in between standard unsteady RANS and detached-eddy simulation. These methods require three-dimensional unsteady calculations using a very small time step and the aim is to make these methods amenable to complex configurations at affordable costs.

Acknowledgements

The author is grateful to Drs. Keith Weinman, Bernhard Eisfeld, Matthias Orlt, Volker Hannemann, Ante Soda, Stefan Melber-Wilkending, Gert Lube, Michael Leschziner and Cord C. Rossow for valuable discussions and to Dr. Christian Gleyzes for informations regarding the A-airfoil. Moreover, the valuable suggestions of the reviewers are gratefully acknowledged.

References

[1] P.S. Granville, A modified van Driest formula for the mixing length of turbulent boundary layers in pressure gradients, J. Fluids Eng. 111 (1989) 94–97.
[2] P.A. Durbin, S.E. Belcher, Scaling of adverse-pressure-gradient boundary layers, J. Fluid Mech. 238 (1992) 699–722.
[3] M. Wang, P. Moin, Dynamic wall modeling for large-eddy simulation of complex turbulent flows, Phys. Fluids 14 (2002) 2043–2051.
[4] N.T. Frink, Tetrahedral unstructured Navier–Stokes method for turbulent flows, AIAA J. 36 (1998) 1975–1982.
[5] T. Rung, Formulation of universal wall boundary conditions for transport equation turbulence models, Technical Report, Hermann-Föttinger-Institut, Technische Universität Berlin, 1999.
[6] E. Goncalves, R. Houdeville, Reassessment of the wall functions approach for RANS computations, Aerosp. Sci. Technol. 5 (2001) 1–14.
[7] W. Vieser, T. Esch, F.R. Menter, Heat transfer predictions using advanced two-equation turbulence models, Technical Report, CFX Technical Memorandum CFX-VAL10/0602, 2002.
[8] G. Kalitzin, G. Medic, G. Iaccarino, P. Durbin, Near-wall behaviour of RANS turbulence models and implication for wall functions, J. Comput. Phys. 204 (2005) 265–291.
[9] G. Medic, G. Kalitzin, G. Iaccarino, E. van der Weide, Adaptive wall functions with applications, AIAA Paper 2006-3744.
[10] E.R. van Driest, Turbulent boundary layer in compressible fluids, J. Aeronaut. Sci. 18 (1951) 145–160.
[11] D.C. Wilcox, Turbulence Modeling for CFD, DWC Industries, La Canada, 1998.
[12] B. Mohammadi, G. Puigt, Wall-laws for high speed flows over adiabatic and isothermal walls, Technical Report, INRIA, Rapport de recherche no. 3948, 2000.
[13] P.R. Spalart, S.R. Allmaras, A one-equation turbulence model for aerodynamics flows, AIAA Paper 1992-0439.
[14] J.R. Edwards, S. Chandra, Comparison of eddy viscosity-transport turbulence models for three-dimensional, shock separated flowfields, AIAA J. 34 (1996) 756–763.
[15] F.R. Menter, Zonal two equation k/ω turbulence models for aerodynamic flows, AIAA Paper 1993-2906.
[16] J.C. Kok, Resolving the dependence on freestream values for the k/ω turbulence model, AIAA J. 38 (2000) 1292–1295.
[17] T. Rung, H. Lübcke, M. Franke, L. Xue, F. Thiele, S. Fu, Assessment of explicit algebraic stress models in transonic flows, in: Engineering Turbulence Modelling and Experiments 4, Proceedings of the 4th International Symposium on Engineering Turbulence Modelling and Measurements, Corsica, France, 1999, pp. 659–668.
[18] S. Wallin, A.V. Johansson, An explicit algebraic Reynolds stress model for incompressible and compressible turbulent flows, J. Fluid Mech. 403 (2000) 89–132.
[19] M.D. Tidriri, Domain decomposition for compressible Navier–Stokes equations with different discretizations and formulations, J. Comput. Phys. 119 (1995) 271–282.
[20] T. Knopp, G. Lube, R. Gritzki, M. Rösler, A near-wall strategy for buoyancy-affected turbulent flows using stabilized FEM with applications to indoor air flow simulation, Comput. Methods Appl. Mech. Eng. 194 (2005) 3797–3816.
[21] T. Knopp, A new adaptive wall-function method for subsonic and transonic turbulent flows, Technical Report, DLR IB 224-2005 A 14, 2005.
[22] D.B. Spalding, A single formula for the law of the wall, J. Appl. Mech. 28 (1961) 455–457.
[23] T. Alrutz, Hybrid grid adaptation in TAU, in: N. Kroll, J.K. Fassbender (Eds.), MEGAFLOW – Numerical Flow Simulation for Aircraft Design, Notes on Numerical Fluid Mechanics and Multidisciplinary Design, vol. 89, Braunschweig, 2005, pp. 109–115.
[24] D.J. Mavriplis, A. Jameson, L. Martinelli, Multigrid solution of the Navier–Stokes equations on triangular meshes, Technical Report, ICASE-report No. 89-35, 1989.
[25] A. Jameson, Transonic flow calculations, Technical Report, MAE Report 1651, Princeton University, 1983.
[26] K. Wieghardt, W. Tillman, On the turbulent friction layer for rising pressure, in: D.E. Coles, E.A. Hirst (Eds.), Computation of Turbulent Boundary Layers – 1968 AFOSR-IFP-Stanford Conference, vol. II, Thermosciences Division, Department of Mechanical Engineering, Stanford University, 1969, pp. 98–123.
[27] H. Schlichting, Boundary-Layer Theory, McGraw-Hill, New York, 1979.
[28] P.H. Cook, M.A. McDonald, M.C.P. Firmin, Aerofoil RAE 2822 – Pressure distributions and boundary layer and wake measurements, Technical Report, AGARD Advisory Report AR-138, 1979, pp. A6.1–A6.77.
[29] C. Gleyzes, Opération décrochage – Résultats des essais à la soufflerie F2, Technical Report, RT-DERAT 55/4004 DN, ONERA, 1988.
[30] C. Gleyzes, Opération décrochage – Résultats de la 2ème campagne d'essais à F2 – Mesures de pression et vélocimétrie laser, Technical Report, RT-DERAT 55/5004 DN, ONERA, 1989.
[31] F.R. Menter, M. Kuntz, R. Bender, A scale-adaptive simulation model for turbulent flow predictions, AIAA Paper 2003-0767.